

ORIGINAL ARTICLE

Open Access



# Connectivity related to major brain functions in Alzheimer disease progression: microstructural properties of the cingulum bundle and its subdivision using diffusion-weighted MRI

Mattia Ricchi<sup>1,2</sup>, Guido Campani<sup>3</sup>, Anastasiia Nagmutdinova<sup>4</sup>, Villiam Bortolotti<sup>4</sup>, Danilo Greco<sup>5,6</sup>, Carlo Golini<sup>7</sup>, James Grist<sup>8</sup>, Leonardo Brizi<sup>7\*</sup>  and Claudia Testa<sup>2,7</sup>

## Abstract

**Background** The cingulum bundle is a brain white matter fasciculus associated with the cingulate gyrus. It connects areas from the temporal to the frontal lobe. It is composed of fibers with different terminations, lengths, and structural properties, related to specific brain functions. We aimed to automatically reconstruct this fasciculus in patients with Alzheimer disease (AD) and mild cognitive impairment (MCI) and to assess whether trajectories have different microstructural properties in relation to dementia progression.

**Methods** Multi-shell high angular resolution diffusion imaging—HARDI image datasets from the "Alzheimer's Disease Neuroimaging Initiative"—ADNI repository of 10 AD, 18 MCI, and 21 cognitive normal (CN) subjects were used to reconstruct three subdivisions of the cingulum bundle, using a probabilistic approach, combined with measurements of diffusion tensor and neurite orientation dispersion and density imaging metrics in each subdivision.

**Results** The subdivisions exhibit different pathways, terminations, and structural characteristics. We found differences in almost all the diffusivity metrics among the subdivisions ( $p < 0.001$  for all the metrics) and between AD versus CN and MCI versus CN subjects for mean diffusivity ( $p = 0.007$ – $0.038$ ), radial diffusivity ( $p = 0.008$ – $0.049$ ) and neurite dispersion index ( $p = 0.005$ – $0.049$ ).

**Conclusion** Results from tractography analysis of the subdivisions of the cingulum bundle showed an association in the role of groups of fibers with their functions and the variance of their properties in relation to dementia progression.

**Relevance statement** The cingulum bundle is a complex tract with several pathways and terminations related to many cognitive functions. A probabilistic automatic approach is proposed to reconstruct its subdivisions, showing different microstructural properties and variations. A larger sample of patients is needed to confirm results and elucidate the role of diffusion parameters in characterizing alterations in brain function and progression to dementia.

Mattia Ricchi and Guido Campani contributed equally to this work.

\*Correspondence:

Leonardo Brizi

[Leonardo.brizi2@unibo.it](mailto:Leonardo.brizi2@unibo.it)

Full list of author information is available at the end of the article



© The Author(s) 2025. **Open Access** This article is licensed under a Creative Commons Attribution 4.0 International License, which permits use, sharing, adaptation, distribution and reproduction in any medium or format, as long as you give appropriate credit to the original author(s) and the source, provide a link to the Creative Commons licence, and indicate if changes were made. The images or other third party material in this article are included in the article's Creative Commons licence, unless indicated otherwise in a credit line to the material. If material is not included in the article's Creative Commons licence and your intended use is not permitted by statutory regulation or exceeds the permitted use, you will need to obtain permission directly from the copyright holder. To view a copy of this licence, visit <http://creativecommons.org/licenses/by/4.0/>.

### Key Points

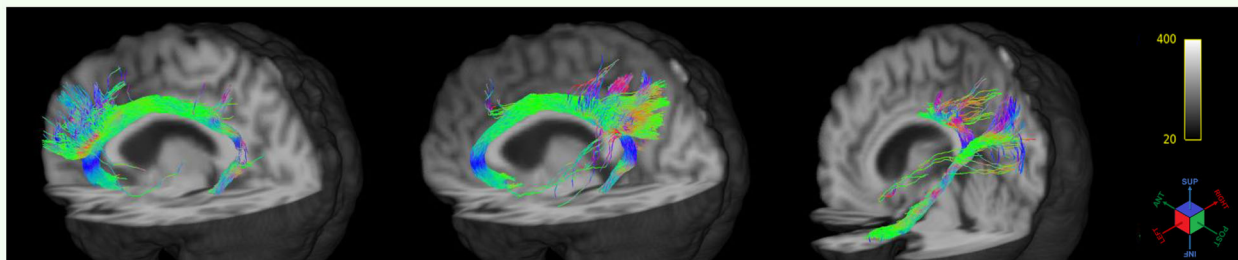
- The microstructure of the cingulum bundle is related to brain cognitive functions.
- A probabilistic automatic approach is proposed to reconstruct the subdivisions of the cingulum bundle by diffusion-weighted images.
- The subdivisions showed different microstructural properties and variations in relation to the progression of dementia.

**Keywords** Alzheimer disease, Brain, Cognitive dysfunction, Diffusion magnetic resonance imaging, White matter

### Graphical Abstract

## Connectivity related to major brain functions in Alzheimer disease progression: microstructural properties of the cingulum bundle and its subdivision using diffusion-weighted MRI

ESR  
EUROPEAN SOCIETY  
OF RADIOLOGY



- The reconstruction of the cingulum bundle is related to major brain functions.
- Its subdivisions exhibit different pathways, terminations, and structural characteristics.
- There are differences in diffusivity metrics among the subdivisions and also between Alzheimer's disease patients and control subjects for some metrics.

3D rendering of the streamlines of the three subdivisions of the cingulum bundle: subgenual (left), the retrosplenial (middle), and parahippocampal (right).

**The cingulum bundle is a complex tract with several pathways and terminations related to many functions. We propose a probabilistic automatic approach to reconstruct its subdivisions, showing different microstructural properties and variations with the progression of dementia**

European  
Radiology  
EXPERIMENTAL

**Eur Radiol Exp (2025) Ricchi M, Campani G, Nagmutdinova A et al;  
DOI: 10.1186/s41747-025-00570-5**

### Background

Diffusion-weighted magnetic resonance imaging (MRI) tractography is a noninvasive method used to identify anatomical connections in the brain by characterizing the water motion within the tissue. This technique is very sensitive to the presence and the orientation of fibers in the brain. If the orientation is estimated, the connections within the entire brain or between specific regions, *a priori* supposed to be connected, can be reconstructed. Several methods for the reconstruction of tracts have been developed, classified as deterministic or probabilistic [1].

Deterministic tractography algorithms assume a unique fiber orientation in each voxel and provide a single pathway emanating from each seed point; however, this approach is limited by the errors and uncertainty related to the image estimate, which may incorrectly identify the principal direction [2]. To overcome this limitation, probabilistic tractography was introduced, where a large

distribution of possible trajectories is generated from each seed [2]. Although computationally more costly, it takes into account the fact that within the unit of spatial resolution (the voxel), more than one axon is present, not necessarily running parallel. Moreover, probabilistic tractography considers the possible inaccuracy of the model used for representing the diffusion signal and the error that affects the experimental measures [3].

Whole brain tractography can be used to reconstruct fiber bundles through seeding from all white matter placed throughout the brain [4]. Nevertheless, if a specific connection (a single tract) has to be reconstructed because of an *a priori* hypothesis, the reconstruction procedure can be performed with higher accuracy by starting from a seed point that defines a specific region of interest (ROI). Typically, these ROIs are defined either by the user or can be defined by an atlas to reduce operator dependence [5].

Here, we consider the probabilistic tractography of the cingulum bundle (CB), a highly complex tract whose structure and functions are not yet fully identified. Initial studies were conducted on rats and nonhuman primates using axonal tracers [6, 7]. Located in the medial zone of the brain, CB forms an arc connecting the parahippocampal cortex to the frontal lobe, passing through the cingulate cortex [8–10]. It is composed of short fibers within the cingulate cortex, medium-length fibers efferent and afferent to the cingulate cortex, and long fibers spanning the entire arc, each group connecting different areas. Although they all belong to the CB, each is associated with a diversity of functions [11], including emotional, reward, and motivational processes, pain processes, motor functions, conflict processes, and memory [11–13]. Tractography in humans rarely describes the complexity of CB. In the literature, it is often depicted as a single entity, uninterrupted from the temporal to the frontal lobe [14]. Correlational studies between the bundle and its associated functions are conducted by dividing the tract into different segments [15]. This approach does not allow the isolation of individual groups of fibers with common terminations, which can explain which parts of the CB are privileged for specific functions.

Recently, some attempts have been made to reconstruct different subdivisions [16], in one case having the reference standard of human brain dissections and using fiber tracking based on a high directional sampling of diffusion imaging space to achieve increased resolution of underlying white matter geometry [17]. Each subdivision is composed of fibers sharing common terminations. Moreover, the various subdivisions have different paths, but their surfaces overlap in some regions of the CB. Tractography studies have observed significant differences in microstructural properties among the various fiber populations of the different subdivisions. These differences could be attributed to the distinct functions that these subdivisions need to optimize [18, 19].

To capture these differences, a probabilistic tractography approach is better than a deterministic one since the latter has many limitations such as the inability to resolve kissing/crossing fibers. For a highly resolved reconstruction of tracts, a “high angular resolution diffusion imaging” (HARDI) acquisition protocol [20] allows the use of innovative high-order crossing fiber models, such as constrained spherical deconvolution [21] and multi-shell multi-tissue constrained spherical deconvolution [22]. Recent literature has proposed a probabilistic constrained-spherical deconvolution tractography to provide a white matter atlas of tracts, including the CB reconstruction into two subdivisions [23]. Multi-shell HARDI acquisition protocols allow the calculation of additional quantitative metrics to the standard diffusion

tensor imaging (DTI) model, quantifying the deviation from the Gaussian behavior assumed in the DTI model. The “neurite orientation dispersion and density imaging” (NODDI) model proposed by Zhang et al [24] is a clinically feasible technique to estimate *in vivo* neurite orientation dispersion and density imaging evaluation. The technique combines a three-compartment tissue model with at least two-shell HARDI protocol, which calculates neurite density and orientation dispersion that can resolve two factors contributing to fractional anisotropy (FA).

The role of the CB can be of particular interest in neurodegenerative diseases whose symptoms are related to a deficit of memory, visuospatial abilities and attention, and executive functions. Among them, mild forms of dementia, like mild cognitive impairment (MCI) that can progress into Alzheimer disease (AD), present behavioral disturbances, which are considered due to dysconnectivity of specific white matter tracts [25, 26]. There is a concerted effort to find biomarkers that can predict the progression from MCI toward AD as they could be targets for possible therapies. The CB is potentially involved in the process of white matter disconnections associated with behavioral impairment in dementia. Few studies have specifically explored dysconnectivity [27–29] with DTI data from local hospitals or free databases, with the number of diffusion gradients directions from 12 to 41 using an ROI- or voxel-based approach and without attempting a specific CB reconstruction. Microscopic white matter changes with aging, and AD can be probed using advanced diffusion MRI methods [30, 31], in particular DTI or NODDI metrics.

The “Alzheimer’s Disease Neuroimaging Initiative” (ADNI) repository (<http://adni.loni.usc.edu/>) has a small group of data in the ADNI3 repository, acquired with a multi-shell HARDI protocol in MCI, AD, and cognitively normal (CN) subjects. This is the only dataset known in literature with these technically and clinically advanced characteristics.

Our primary aim was to define an automated protocol that identifies three subdivisions of the CB and to verify the presence of fiber populations with different microstructural properties using a probabilistic tractography MRI technique. In the current literature, no study has analyzed the CB by determining its anatomical subdivisions using a multi-shell HARDI protocol, allowing the modeling of three tissue compartments (gray matter, white matter, and cerebrospinal fluid) with different diffusion characteristics to better reconstruct tracts using only the white matter compartment data. A second aim was to assess whether the CB in its subdivisions, once automatically reconstructed, has different microstructural properties in CN subjects, MCI, and AD patients. Overall, this work aimed to give a robust instrument to evaluate brain connectivity involving the CB, which can be used for

the evaluation of microstructural changes in the progression of dementia.

## Methods

### Subjects and MRI protocol

The inclusion criterion was a multi-shell HARDI acquisition protocol for DTI with at least 60 gradient directions for the maximum  $b$ -value. We included 49 participants: 5 middle-aged CN subjects, aged  $54.6 \pm 2.6$  years (mean  $\pm$  standard deviation), 2 males and 3 females; 16 older CN subjects, aged  $74.4 \pm 8.4$  years, 6 males and 10 females, 18 MCI patients, aged  $75.8 \pm 5.4$  years, 7 males and 11 females; and 10 AD, aged  $76.1 \pm 7.9$  years, 4 males and 6 females from the ADNI database. Subjects completed the Mini-Mental State Exam (MMSE) and Montreal cognitive assessment (MoCA) [32, 33]. The characteristics of CN, MCI, and AD subjects are shown in detail in Table 1. Sagittal 3D T1-weighted anatomical images were acquired. Details on technical parameters are provided in Supplementary materials, Methods).

### DTI processing and image registration

DTI data were preprocessed using a self-developed automated workflow based on software packages freely available as part of the Oxford Functional Magnetic Resonance Imaging Software Library (FSL) [34] version 6, MRtrix3 version 3.0.2 [35, 36] and using a recent tool Synb0-DISCO [37, 38] (see Supplementary materials, Methods).

Microstructural properties of the brain tissue were characterized by estimating voxel FA, mean diffusivity (MD), and radial diffusivity (RD) using FSL. The implementation of the Bingham-NODDI model was performed by using the Diffusion Microstructure Imaging in Python (Dmipy) package [39] to calculate the NODDI metrics: tissue volume fraction,  $\beta$ -fraction, neurite dispersion index (NDI), and orientation dispersion index (ODI) (see Supplementary materials, Methods).

The image alignments to the diffusion space and to the T1 space have been performed by FSL registration tools both for linear and nonlinear registration (see Supplementary materials, Methods).

### CB tract reconstruction: methods

Tractography was performed by *tckgen* which generates streamlines using a first-order integration over fiber orientation distributions (*iFOD2*) approach [40].

Firstly, the CB reconstruction was performed in the middle-aged CN group to identify the ROIs for the automatic reconstruction, to understand the feasibility of the method, and to explore the robustness of the approach. Then, the methodology was applied to the three groups of subjects. Streamline integration utilized the *iFOD2* algorithm starting from two-dimensional ROIs. “Include” and “exclude” ROIs were used. For each hemisphere, we reconstructed three different subdivisions of the CB as Jones et al described in their work [16]. We named the three tracts as follows: subgenual cingulum (SGC); retrosplenial cingulum (RSC); and parahippocampal cingulum (PHC).

Details about the reconstruction of the subdivisions in the middle-aged CN group are reported in Supplementary material, Methods—Supplemental Fig. S1, Table S1, Fig S2.

### Cingulum bundle tract reconstruction: application to subjects' groups

Once the ROIs and the masks were defined in the MNI space (see Supplemental material, Methods), the methods for the CB reconstructions were applied to the subdivisions, across subjects. For new subjects, the ROIs and the masks were registered from the MNI space in their own diffusion space, and streamlines were constructed for each of the three subdivisions of the CB.

**Table 1** Subjects and cognitive scores characteristics

	Number (females)	Age, years (mean $\pm$ standard deviation)	MMSE <sup>a</sup>	MoCA <sup>b</sup>
Cognitively normal (CN)	16 (10)	74.4 $\pm$ 8.4	28.4 $\pm$ 1.4	25.2 $\pm$ 2.0
Mild cognitive impairment (MCI)	18 (11)	75.8 $\pm$ 5.4	27.2 $\pm$ 1.9	21.1 $\pm$ 4.2
Alzheimer disease (AD)	10 (6)	76.1 $\pm$ 7.9	23.7 $\pm$ 4.8	16.0 $\pm$ 3.8
$\chi^2$ ( $p$ -value)	0.992			
ANOVA ( $p$ -value)		0.801	0.001	< 0.001
Tukey HSD ( <i>post hoc</i> test)				
AD < CN (adjusted $p$ -value)			< 0.001	< 0.001
AD < MCI (adjusted $p$ -value)			0.015	0.009
MCI < CN (adjusted $p$ -value)			0.453	0.006

MMSE Mini-Mental State Exam, MoCA Montreal cognitive assessment

<sup>a</sup> MMSE was available for 9 out of 10 AD, for 16 out of 19 MCI

<sup>b</sup> MoCA was available for 7 out of 10 AD, for 15 out of 19 MCI

The alignment of the ROIs in the diffusion space was checked and in no case we had to re-define them. The resulting streamlines were then trimmed according to the boundaries defined by the mask, which was binarized and multiplied for the corresponding reconstructed tract, following a method already validated [5, 41].

### Statistical analysis

An ANOVA was used to control groups' age, with  $p = 0.050$  as a cutoff for significance. The sex distribution in the subjects' groups was tested using a  $\chi^2$  test. Tracts were reconstructed for all 49 participants. The mean values within each tract subdivision of DTI and NODDI metrics were then compared and analyzed. Firstly, the normality and homogeneity of variances of the distributions of FA, MD, RD, tissue volume fraction,  $\beta$ -fraction, NDI, and ODI values for each group and each subdivision were tested using the Shapiro-Wilks and Levene's tests. Then, the distributions of microstructural values were compared among groups, tract subdivisions of the same type but located in different hemispheres (side), as well as the distributions of values for different tracts. This compatibility test was performed using the three-way factor ANOVA test. In these cases, the *post hoc* test, Tukey's honestly significant difference (HSD) test, was employed. *Post hoc* tests control the family-wise error rate by the Benjamini–Hochberg step-up procedure [42]. A Pearson correlation analysis was performed for the mean values within each tract subdivision of all the diffusion metrics and MoCA and MMSE scores. Python libraries were used for statistical analysis (Python 3.11.9).

### Results

The code of the pipeline, the MNI ROIs and masks have been shared in a Github repository ([https://github.com/MattRicchi/Cingulum\\_Bundle\\_tractography.git](https://github.com/MattRicchi/Cingulum_Bundle_tractography.git)).

The three groups—CN, MCI, and AD—did not differ significantly in age (ANOVA,  $p = 0.801$ ) or gender ( $\chi^2$ ,  $p = 0.992$ ) but did differ in MMSE (ANOVA:  $p = 0.001$ )

and in MoCA (ANOVA,  $p < 0.001$ ). The *post hoc* analysis showed that there is a significant difference between AD and CN and between AD and MCI for the MMSE score as well as between all the pairs of subjects' groups for the MoCa score. Demographic results are shown in Table 1.

The use of Synb0-DISCO was successfully applied to all the diffusion-weighted images and results were evaluated as optimal after performing the image difference between pre- and post-correction, and visually assessing that the regions affected by distortions were those corrected by the algorithm (Supplemental Fig. S3).

Tracts were reconstructed for all the subjects except for one hemispherical SGC subdivision in one patient of the AD group. This failure was thought to be due to highly enlarged ventricles and specifically with a substantial asymmetry in the compartments. An example of the reconstruction of the three subdivisions for one middle-aged CN case is shown in Fig. 1.

### Tractography

The SGC subdivision starts anteriorly from the lateral orbitofrontal cortex, medial orbitofrontal cortex, and rostral cingulate cortex. It extends superiorly to the corpus callosum, slightly shifting towards the sagittal plane. The terminations of the bundle are around the posterior cingulate cortex and near the ventral precuneus area. The RSC also originates from the rostral cingulate cortex, but in a more superior position, at the level of the most anterior point of the corpus callosum. The bundle then extends above the corpus callosum and terminates in the isthmus of the cingulate gyrus. The PHC subdivision connects the hippocampal and parahippocampal areas up to the region of the cortex between the precuneus and the isthmus of the cingulate gyrus (Fig. 2).

### Microstructural values

Figures 3 and 4 show the boxplots of the distributions of FA, MD, and RD values and for the NODDI metrics respectively for the three subdivisions and the three

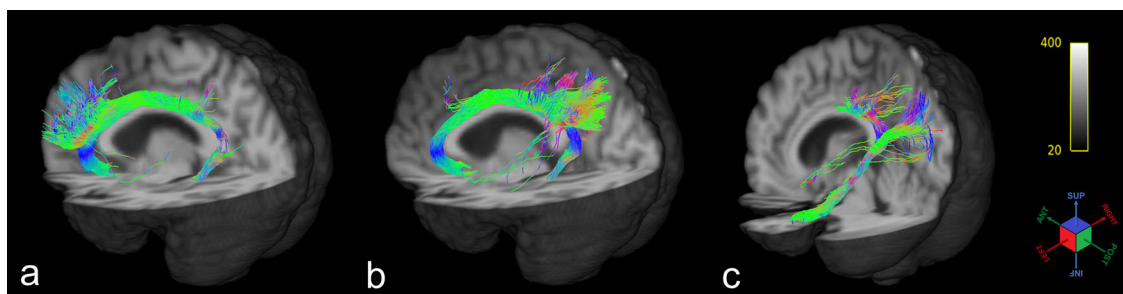


**Fig. 1** Three-dimensional rendering of the streamlines of the three subdivisions of the cingulum bundle for one middle-aged cognitive normal case (female, 53-y.o.): **a** the subgenual subdivision without the application of the mask; **b** the retrosplenial subdivision without the application of the mask; **c** the parahippocampal subdivision without the application of the mask (streamlines that may be false-positive findings are visible as isolated fibers)

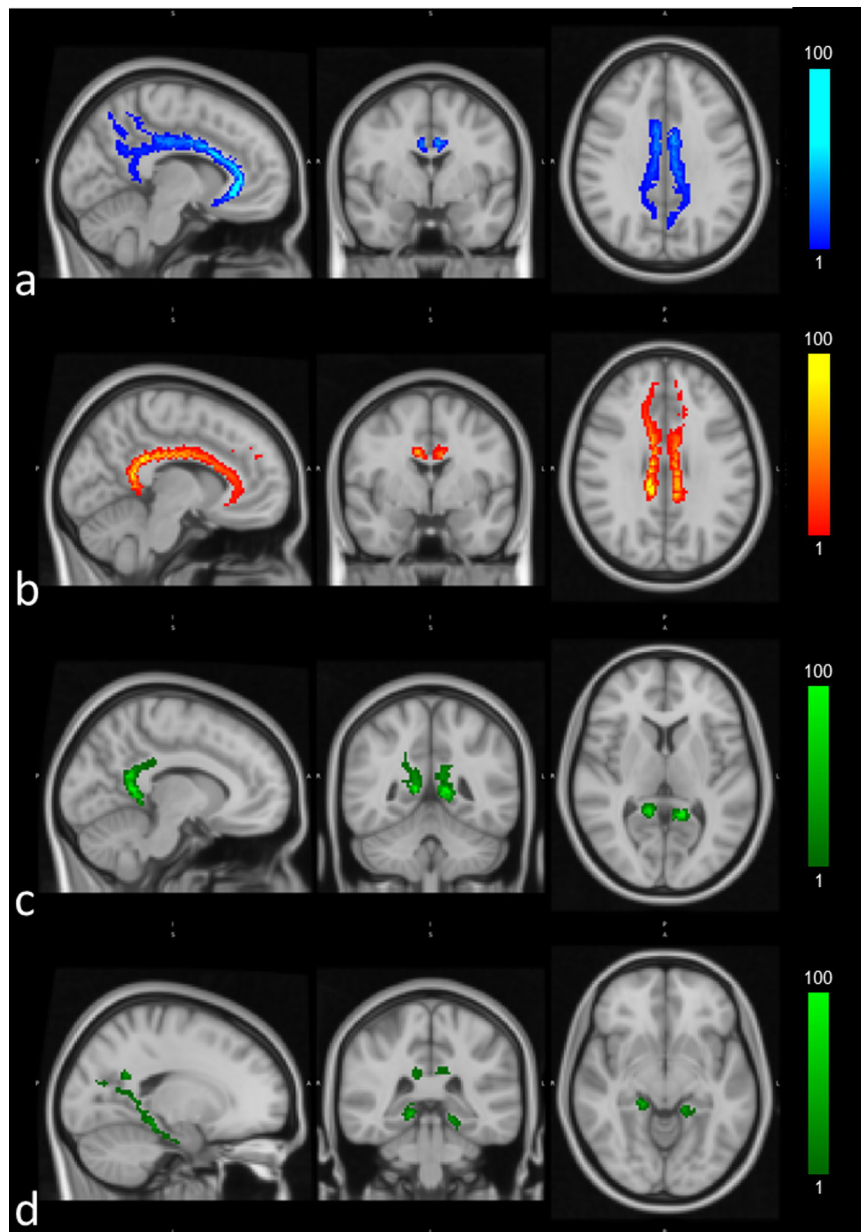


**Fig. 2** Orthogonal view of the three subdivisions of the CB reconstructed for one middle-aged cognitive normal case (female, 53-y.o.) aligned to the Montreal Neurological Institute atlas. The signal (fiber orientation distribution function) is normalized between 0 and 100. **a** The SGC subdivision shows this portion of the CB going from the orbitofrontal cortex to the rostral cingulate cortex, extending above the corpus callosum. The terminations of the bundle are around the posterior cingulate cortex and near the ventral precuneus area. **b** The RSC originates from the rostral cingulate cortex, the level of the most anterior point of the corpus callosum extending above the corpus callosum and terminating in the isthmus of the cingulate gyrus. **c, d** The PHC subdivision connects the hippocampal and parahippocampal areas (**d**) up to the region of the cortex between the precuneus and the isthmus of the cingulate gyrus (**c**). CB, Cingulum bundle; PHC, Parahippocampal cingulum; RSC, Retrosplenial cingulum; SGC, Subgenual cingulum

groups of subjects. The normality and homogeneity of variances tests suggested that the data for each group of patients did not significantly deviate from a normal distribution ( $p = 0.116$  for AD,  $p = 0.699$  for MCI, and  $p = 0.246$  for CN).

A three-way ANOVA test was performed for FA, MD, and RD (Table 2). A significant effect was found on all the DTI metrics for the subdivisions and groups: FA subdivision effect,  $F = 90.58$ ,  $p < 0.001$ ; FA group effect,  $F = 11.83$ ;  $p < 0.001$ ; MD subdivision effect,  $F = 61.34$ ,

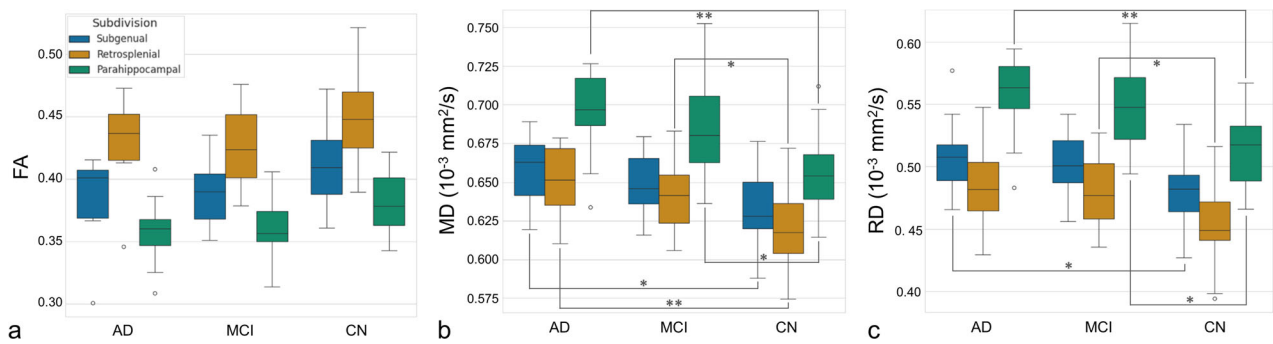


**Fig. 3** Box-plots of the distribution FA (a), MD (b), and RD (c) values for the three subdivisions of the cingulum bundle and the three groups of subjects. \* indicates significant differences with a  $p$ -value < 0.05; \*\* indicates significant differences with a  $p$ -value < 0.01. AD, Alzheimer disease; CN, Cognitive normal; FA, Fractional anisotropy; MCI, Mild cognitive impairment; MD, Mean diffusivity; RD, Radial diffusivity

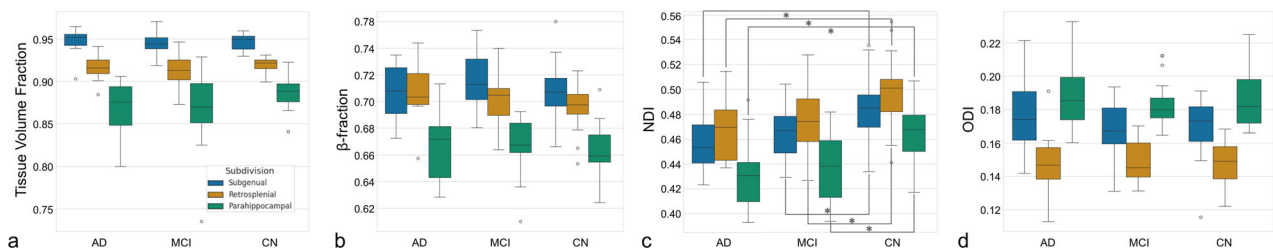


**Fig. 4** Box-plots of the distribution total volume fraction (a),  $\beta$ -fraction (b), NDI (c), and ODI (d) values for the three subdivisions of the cingulum bundle and the three groups of subjects. \* indicates significant differences with a  $p$ -value < 0.05; \*\* indicates significant differences with a  $p$ -value < 0.01. AD, Alzheimer disease; CN, Cognitive normal; MCI, Mild cognitive impairment; NDI, Neurite density index; ODI, Orientation dispersion index

$p < 0.001$ ; MD group effect,  $F = 31.25$ ,  $p < 0.001$ ; RD subdivision effect,  $F = 93.09$ ,  $p < 0.001$ ; and RD group effect,  $F = 25.96$ ,  $p < 0.001$ .

In addition, the same test was performed for tissue volume fraction,  $\beta$ -fraction, NDI, and ODI (Table S2). A significant effect for subdivision was found on all the NODDI metrics. In addition, a significant group effect was found for tissue volume fraction and NDI: tissue volume fraction subdivision effect,  $F = 187.01$ ,  $p < 0.001$ ; tissue volume fraction group effect,  $F = 3.72$ ,  $p = 0.026$ ;  $\beta$ -fraction subdivision effect,  $F = 75.80$ ,  $p < 0.001$ ; NDI subdivision effect,  $F = 39.74$ ,  $p < 0.001$ ; NDI group effect,  $F = 25.86$ ,  $p < 0.001$ ; and ODI subdivision effect,  $F = 74.15$ ,  $p < 0.001$ . A side effect (and a causal interaction effect between side and subdivisions) was found for  $\beta$ -fraction ( $F = 8.46$ ,  $p < 0.004$ ). Being the only diffusion metric sensitive to the side effect, it was not taken into account in this study, deserving further investigation. For this reason, microstructural parameters were then averaged between left and right.

*Post hoc* analyses were performed independently for the group effect and for the subdivision effect given the results of ANOVA. The Tukey's HSD test was performed applying the Benjamini–Hochberg correction. Table 3

and Supplemental Table S3 show the results for group *post hoc* comparison for the DTI and NODDI metrics, respectively. Table 3 and Supplemental Table S3 show that the lowest effect size relative to the AD *versus* MCI is FA in the RSC subdivision (effect size = 0.11).

The *post hoc* analysis showed that FA and tissue volume fraction were not significantly different for the group effect. MD, RD, and NDI showed a significant effect for the comparison AD *versus* CN in almost all the subdivisions and for the comparison MCI *versus* CN in the RSC subdivision.

The same *post-hoc* analysis was performed considering the subdivisions for the DTI and NODDI metrics respectively (Table 4 and Supplemental Table S4). Almost all the diffusion metrics were significant for the subdivision effect. Only for the comparisons of RSC *versus* SGC (in each group), diffusion metrics result in less sensitive.

Correlation analysis between diffusion metrics and MoCA scores for each tract subdivision showed no statistically significant results after the correction for multiple comparisons. Nevertheless, the MD and NDI values for the PHC subdivision correlated with MoCA score with an uncorrected  $p = 0.030$  and  $p = 0.049$ , respectively; for the same subdivision RD had  $p = 0.041$ . The RSC

**Table 2** Three-way ANOVA results for the three metrics: fractional anisotropy, mean diffusivity, and radial diffusivity

Fractional anisotropy			Mean diffusivity			Radial diffusivity		
Effect	F	p-value	Effect	F	p-value	Effect	F	p-value
Subdivision (SGC, RSC, PHC)	90.58	< <b>0.001</b>	Subdivision (SGC, RSC, PHC)	61.34	< <b>0.001</b>	Subdivision (SGC, RSC, PHC)	93.09	< <b>0.001</b>
Side (left, right)	0.30	0.579	Side (left, right)	0.96	0.329	Side (left, right)	0.03	0.864
Group (AD, MCI, CN)	11.83	< <b>0.001</b>	Group (AD, MCI, CN)	31.25	< <b>0.001</b>	Group (AD, MCI, CN)	25.96	< <b>0.001</b>
Subdivision : Group	0.17	0.953	Subdivision : Group	0.42	0.792	Subdivision : Group	0.26	0.901
Subdivision : Side	1.20	0.301	Subdivision : Side	1.70	0.184	Subdivision : Side	1.49	0.226
Side : Group	0.66	0.513	Side : Group	0.24	0.789	Side : Group	0.38	0.685
Subdivision : Tract : Side	0.05	0.995	Subdivision : Tract : Side	0.01	0.999	Subdivision : Tract : Side	0.02	0.999

AD Alzheimer disease, CN Cognitively normal, MCI Mild cognitive impairment, PHC Parahippocampal cingulum, RSC Retrosplenial cingulum, SGC Subgenual cingulum  
In bold the significant adjusted  $p$ -values ( $< 0.05$ )

subdivision MD was significant with an uncorrected  $p$ -value of 0.047.

Correlation analysis between diffusion metrics and MMSE scores was explored even if the Tukey HSD *post hoc* test did not reach significant results for the MCI versus CN comparison. Results were not statistically significant after the correction for multiple comparisons. Nevertheless, the MD and NDI values for the PHC subdivision correlated with the MMSE score with an uncorrected  $p = 0.027$  and  $p = 0.034$ , respectively.

## Discussion

We have proposed an automatic protocol to explore the connectivity of the CB, retracing the steps reported by Jones et al [16] suitable to reconstruct the three subdivisions: SGC, RSC, and PHC. Differently from these authors, we used a probabilistic approach ensuring a more robust, comprehensive, and reliable representation of the fibers. Successive research both in humans and macaques [17, 43] has compared CB reconstruction with brain dissection, which, even if not wholly safe from false findings, is the reference standard for tractography. Hailbronner and Haber [43] grouped the fibers of CB into four zones based on their specific connections: subgenual, rostral dorsal, caudal dorsal, and temporal.

The presence of fibers that do not originate or terminate in the cingulate cortex, has reshaped the understanding of the CB. It is not seen solely as fibers associated with the cingulate gyrus, but it is a multilayered network of connection with short, medium, and long-length fibers that share different patterns of connection. Wu et al [17] performed a deterministic tractography compared with brain dissections. According to this work, the CB should be divided into five components: CB-I to CB-V briefly are analogous to our SGC, RSC, and PHC; CB-II and CB-III corresponding to our RSC; CB-IV, a minor subcomponent from the superior parietal lobule and precuneus to the supplementary and premotor areas in the frontal region of

the brain has not an exact correspondence to our subdivisions. Our approach was not suitable for reproducing these five subdivisions even though the three subdivisions—SGC, RSC, and PHC—can be associated with compositions of the five subdivisions obtained through dissection reported by Wu et al [17]. Nevertheless, our approach relies on a multishell HARDI protocol, which, combined with a multi-tissue probabilistic approach, has been demonstrated to be more robust in the reconstruction of kissing and crossing fibers [2, 40, 44]. Moreover, we have applied a multi-compartment model to calculate diffusion microstructural properties measuring the NODDI metrics.

Our workflow allowed us to reconstruct the CB subdivisions for all the subjects with the exception of one subdivision out of 294 (3 subdivisions, both for the left and right hemispheres and for 49 subjects) due to high asymmetrical enlargement of ventricles. We selected a homogeneous set of data for which the CB reconstruction is clinically relevant and with acquisition parameters of the DTI sequence corresponding to a multi-shell HARDI protocol. The limit of this dataset due to the lack of specific sequences for distortion correction has been successfully overcome by using the Synb0-DISCO tool [38] (Supplemental Fig. S3). This tool opens the opportunity to use many other public data repositories for brain connectivity research, even if the quality of diffusion-weighted images is not optimal for tractography reconstruction.

The workflow can be easily reproduced using the set of ROIs explicitly drawn and registered in the MNI space to make the procedure automatic (Supplemental Fig. S1 and Supplemental Table S1). A definition of a mask (Supplemental Fig. S2) to trim the streamlines for each subdivision has been demonstrated to work efficiently to reduce the few false positives (Fig. 1).

The spatial disposition of the subdivisions is different for each of them. The subgenual subdivision is the most

**Table 3** Post hoc analyses for group differences performed by the Tukey's HSD test applying the Benjamini–Hochberg correction for the adjusted *p*-values

Fractional anisotropy				Mean diffusivity				Radial diffusivity			
Group	Subdivision	Adjusted <i>p</i> -value	Effect size	Group	Subdivision	Adjusted <i>p</i> -value	Effect size	Group	Subdivision	Adjusted <i>p</i> -value	Effect size
AD < CN	SGC	0.169	0.71	AD < CN	SGC	<b>0.019</b>	1.08	AD > CN	SGC	<b>0.049</b>	0.94
AD < MCI	SGC	0.926	0.15	AD > MCI	SGC	0.622	0.40	AD > MCI	SGC	0.833	0.24
MCI < CN	SGC	0.185	0.65	MCI > CN	SGC	0.062	0.83	MCI > CN	SGC	0.070	0.82
AD < CN	RSC	0.347	0.51	AD > CN	RSC	<b>0.009</b>	1.16	AD > CN	RSC	0.052	0.89
AD < MCI	RSC	0.963	0.11	AD > MCI	RSC	0.603	0.41	AD > MCI	RSC	0.941	0.14
MCI < CN	RSC	0.138	0.68	MCI > CN	RSC	<b>0.038</b>	0.89	MCI > CN	RSC	<b>0.047</b>	0.86
AD < CN	PHC	0.077	0.88	AD > CN	PHC	<b>0.007</b>	1.35	AD > CN	PHC	<b>0.008</b>	1.33
AD < MCI	PHC	0.880	0.19	AD > MCI	PHC	0.691	0.31	AD > MCI	PHC	0.737	0.28
MCI < CN	PHC	0.109	0.75	MCI > CN	PHC	<b>0.018</b>	0.99	MCI > CN	PHC	<b>0.018</b>	1.01

AD Alzheimer disease, CN Cognitively normal, MCI Mild cognitive impairment, PHC Parahippocampal cingulum, RSC Retrosplenial cingulum, SGC Subgenual cingulum  
 In bold the significant adjusted *p*-values (< 0.05). Effect size computed as "Cohen's *d*" (small = 0.2; medium = 0.5; large: 0.8)

medial and frontal one; it starts from the lateral-medial orbital cortex and continues above the corpus callosum to the caudal limit of the posterior cingulate cortex and near the ventral precuneus area (Fig. 1a). It can be associated with CB-I described by Wu et al [17]. Due to its position, as suggested by Wu et al, this bundle could be linked to emotional responses to painful stimuli [45], cognitive functions, and verbal memory performance [46]. Its termination inside the precuneus may have a fundamental role in the default mode network, according to Skandalakis et al [47]. Finally, it may be related to the executive function: Bubb et al [15] reviewed the literature reporting correlations between FA and MD and working memory, attention, and executive functions and found that significant results exist only for the anterior and posterior portion of the CB in healthy elderly subjects [48], so precisely the terminations covered by this subdivision.

The RSC subdivision, which wraps around the corpus callosum in a semicircle, is positioned more laterally than the SGC subdivision and can be associated with CB-II and CB-III [15] (Fig. 1b). Due to its connections, this tract could be associated with the response conflict [49] and the motor function [11]. Referring to the study of Fox et al [50], this tract may play a significant role in the performance of demanding cognitive tasks or the integration pathways [50, 51].

The PHC subdivision starts from the precuneus area and the isthmus cingulate cortex, terminating in the temporal lobe near the parahippocampal cortex. It is slightly more lateral than the RSC subdivision (Fig. 1c). This subdivision can be associated with CB-V described by Wu et al [17]. The CB-V is believed to function as a regulating route that facilitates various cognitive abilities, encompassing the transmission of visuospatial, facial, and memory cues from the medial temporal region to the precuneus [47].

In this work, we have shown that the two hemispheres had no statistically significant difference in tensor and NODDI metrics with the exception of  $\beta$ -fraction for all the subdivisions, while for each of the diffusion metrics, there are differences between subdivisions and groups of patients (Table 2 and Supplemental Table S2). The significance of the  $\beta$ -fraction has been neglected in the analysis, deserving a deeper analysis in a larger cohort of healthy subjects.

The three subdivisions have shown highly significant differences for almost all the pair comparisons of FA, RD, tissue volume fraction, and ODI and in the two pair comparisons involving the PHC subdivision of the MD (Table 4 and Supplemental Table S4). FA and tissue volume fraction showed the lowest value for the PHC subdivision, possibly for the high curvature of the tract and for the closeness to the fourth ventricles (Fig. 2c and

**Table 4** *Post hoc* analyses for subdivision differences performed by the Tukey's HSD test applying the Benjamini–Hochberg correction for the adjusted *p*-value

Fractional anisotropy			Mean diffusivity			Radial diffusivity		
Subdivision	Group	Adjusted <i>p</i> -value	Subdivision	Group	Adjusted <i>p</i> -value	Subdivision	Group	Adjusted <i>p</i> -value
RSC > PHC	CN	< <b>0.001</b>	RSC < PHC	CN	< <b>0.001</b>	RSC < PHC	CN	< <b>0.001</b>
SGC > PHC	CN	<b>0.035</b>	SGC < PHC	CN	<b>0.019</b>	SGC < PHC	CN	<b>0.008</b>
RSC > SGC	CN	<b>0.003</b>	RSC < SGC	CN	0.418	RSC < SGC	CN	<b>0.044</b>
RSC > PHC	AD	< <b>0.001</b>	RSC < PHC	AD	<b>0.003</b>	RSC < PHC	AD	< <b>0.001</b>
SGC > PHC	AD	0.202	SGC < PHC	AD	<b>0.019</b>	SGC < PHC	AD	<b>0.019</b>
RSC > PHC	AD	<b>0.021</b>	RSC < SGC	AD	0.781	RSC < SGC	AD	0.238
RSC > PHC	MCI	< <b>0.001</b>	RSC < PHC	MCI	< <b>0.001</b>	RSC < PHC	MCI	< <b>0.001</b>
SGC > PHC	MCI	<b>0.009</b>	SGC < PHC	MCI	< <b>0.001</b>	SGC < PHC	MCI	< <b>0.001</b>
RSC > SGC	MCI	< <b>0.001</b>	RSC < SGC	MCI	0.510	RSC < SGC	MCI	<b>0.047</b>

AD Alzheimer disease, CN Cognitively normal, MCI Mild cognitive impairment, PHC Parahippocampal cingulum, RSC Retrosplenial cingulum, SGC Subgenual cingulum  
In bold the significant adjusted *p*-values (< 0.05)

Fig. 4a, respectively). The RSC subdivision showed the highest FA values, possibly due to the high orientation/low spread of this portion of the CB, and a lower tissue volume fraction with respect to the SGC subdivision, possibly because the RSC is closer to the lateral ventricles. These trends are inversely reflected in the MD and RD trends. Thus, the effort made to reconstruct the CB representing a multilayered network of short, medium, and long-length fibers that share different patterns of connection is useful to characterize the specific microstructural properties of each of them. These results are consistent with findings described by Beckmann et al [11], indicating that each subdivision of the same type identifies populations of fibers with different structural characteristics.

Concerning differences between groups (Table 3 and Supplemental Table S3), we found that FA and tissue volume fraction were not significantly sensitive to CB neurodegeneration for all the subdivisions in this data set. The adjusted *p*-value was close to the significance threshold and corresponds to the comparison of AD *versus* CN for the parahippocampal subdivision. The PHC subdivision was the most impaired in terms of MD RD and NDI for both the comparisons of AD and MCI with CN. The comparisons between AD and CN of MD and NDI values showed significant differences also for SGC and RSC.

Overall, MD, RD, and NDI were the most affected metrics reflecting possible early axonal degeneration. Moreover, the PHC subdivision is the most sensitive to degeneration due to the AD, also considering the trend of correlation between the MoCA and MMSE score and MD, RD, and NDI in this subdivision. This is in line with the fact that the PHC subdivision has its term in the parahippocampal and hippocampal gray matter regions

that are the most affected by degeneration in AD patients [52].

Some limitations can be considered, essentially related to the small number of MCI and AD patients. In fact, although ADNI is the most extensive data repository for neuroimages in dementia, the type of data we have chosen is the best to apply a multi-shell multi-tissue analysis of diffusion-weighted images, but they were few. This may have conditioned the nonsignificant differences between MCI and AD for both the DTI and NODDI metrics. As shown in Table 3, if we consider at least a small effect size of 0.2, a power analysis assesses that a minimum number of 26 MCI *versus* 26 AD patients is needed to detect a statistically significant difference of FA in this comparison. This number would ensure a small effect size for almost all the other metrics comparisons.

An extensive neuropsychological battery of tests to assess a wide range of cognitive functions would be necessary for patients affected with dementia to evaluate which subdivision is primarily sensitive to one specific cognitive impairment and if this evaluation predicts the progression of dementia. Future work will be devoted to applying the presented methodology to datasets with multi-shell HARDI protocol which is already used in the clinical presurgical setting [53, 54].

In conclusion, this study contributes to aligning the CB representation with its anatomical and biological understanding. We have developed a probabilistic tractography protocol using high-resolution diffusion-weighted images for the automatic determination of the three subdivisions of the CB. They exhibited different terminations and pathways with distinct structural characteristics. The overall result plays in favor of future correlational studies in the realm of functions and analyzes specific markers for certain pathologies: the subgenual tract for executive

functions and the default mode network; the retrosplenial tract for motor functions and conflict response processes as well as demanding cognitive tasks or integration pathways; the parahippocampal tract for the transmission of visuospatial, facial, and memory cues.

#### Abbreviations

AD	Alzheimer disease
ADNI	Alzheimer Disease Neuroimaging Initiative
CB	Cingulum bundle
CN	Cognitively normal
DTI	Diffusion tensor imaging
FA	Fractional anisotropy
FSL	Oxford Functional Magnetic Resonance Imaging Software Library
HARDI	High angular resolution diffusion imaging
HSD	Honestly significant difference
MCI	Mild cognitive impairment
MD	Mean diffusivity
MMSE	Mini-Mental State Exam
MNI	Montreal Neurological Institute
MoCA	Montreal cognitive assessment
MRI	Magnetic resonance imaging
NDI	Neurite dispersion index
NODDI	Neurite orientation dispersion and density index
ODI	Orientation dispersion index
PHC	Parahippocampal cingulum
RSC	Retrosplenial cingulum
RD	Radial diffusivity
ROI	Region of interest
SGC	Subgenual cingulum

#### Supplementary information

The online version contains supplementary material available at <https://doi.org/10.1186/s41747-025-00570-5>.

**Additional file 1: Fig. S1.** Three-dimensional rendering of the ROIs used to reconstruct the three subdivisions of the cingulum bundle superimposed in the Montreal Neurological Institute space represented as a surface. ROI 1 (violet) and ROI 2 (teal) were used for the reconstruction of the subgenual subdivision as seed and “include” mode, respectively; ROI 3 (red) and ROI 4 (green) were used for the reconstruction of the retrosplenial subdivision as seed and “include” mode, respectively; ROI 5 (blue), ROI 6 (pink for the left hemisphere and yellow for the right hemisphere), and ROI 4 were used to reconstruct the parahippocampal subdivision as seed, “exclude”, and “include” mode, respectively. *ROI* Region of interest. **Fig. S2.** Orthogonal view of the thresholded (at 1%) overlap of the subdivisions of the cingulum bundle for the five middle-aged cognitive normal case (average representation): subgenual in cyan-blue color map (a); retrosplenial in red-yellow color map (b); and parahippocampal in light-dark green color map (c). The intensity scales are percentages associated to the minimum and maximum of the subjects represented by the overlap of the tracts. **Fig. S3.** (a) Example of axial views of diffusion-weighted images ( $b = 0 \text{ s/mm}^2$ ) before distortion correction; distortions are evident especially in the frontal part of the brain. (b) The same axial view after Synb0-DISCO application and distortions correction, showing the frontal part of the brain restored. (c) The difference between a and b showing at a first glance, regions where the Synb0-DISCO have mostly corrected the distortions. **Table S1.** Coordinates of the center of gravity of the six ROIs and the midsagittal ROI used to reconstruct the subgenual, retrosplenial, parahippocampal subdivision of the cingulum bundle are reported in standard Montreal Neurological Institute space for both hemispheres. **Table S2.** Three-way ANOVA results for four NODDI metrics: tissue volume fraction,  $\beta$ -fraction, neurite dispersion index, and orientation dispersion index. **Table S3.** Post hoc analyses for group differences performed by the Tukey's HSD test applying the Benjamini–Hochberg correction for the adjusted  $p$ -values. **Table S4.** Post

hoc analyses for subdivision differences performed by the Tukey's HSD test applying the Benjamini–Hochberg correction for the adjusted  $p$ -values.

#### Acknowledgements

Data collection and sharing for this project was funded by the "Alzheimer's Disease Neuroimaging Initiative" (ADNI) (National Institutes of Health Grant U01 AG024904) and DOD ADNI (Department of Defense award number W81XWH-12-2-0012). ADNI is funded by the National Institute on Aging, the National Institute of Biomedical Imaging and Bioengineering, and through generous contributions from the following: AbbVie, Alzheimer Association; Alzheimer Drug Discovery Foundation; Araclon Biotech; BioClinica, Inc.; Biogen; Bristol-Myers Squibb Company; CereSpir, Inc.; Cogstate; Eisai Inc.; Elan Pharmaceuticals, Inc.; Eli Lilly and Company; EuroImmun; F. Hoffmann-La Roche Ltd and its affiliated company Genentech, Inc.; Fujirebio; GE Healthcare; IXICO Ltd.; Janssen Alzheimer Immunotherapy Research & Development, LLC.; Johnson & Johnson Pharmaceutical Research & Development LLC.; Lumosity; Lundbeck; Merck & Co., Inc.; Meso Scale Diagnostics, LLC.; NeuroRx Research; Neurotrack Technologies; Novartis Pharmaceuticals Corporation; Pfizer Inc.; Piramal Imaging; Servier; Takeda Pharmaceutical Company; and Transition Therapeutics. The Canadian Institutes of Health Research is providing funds to support ADNI clinical sites in Canada. Private sector contributions are facilitated by the Foundation for the National Institutes of Health ([www.fnih.org](http://www.fnih.org)). The grantee organization is the Northern California Institute for Research and Education, and the study is coordinated by the Alzheimer Therapeutic Research Institute at the University of Southern California. ADNI data are disseminated by the Laboratory for Neuro Imaging at the University of Southern California. No Large Language Models were used in this paper.

#### Author contributions

MR analyzed and interpreted subjects' data, performed statistical analyses, and wrote the manuscript. GC contributed to the conceptualization of the manuscript, preprocessed subjects' data, and wrote the manuscript. CG analyzed the subjects' data and performed statistical analyses. AN contributed to the definition/performance of the statistical analyses and revised the manuscript. VB contributed to the conceptualization of the manuscript and revised it. DG contributed to the conceptualization of the manuscript and revised it. JG contributed to the data analysis for the NODDI model, and he revised the manuscript. LB contributed to the conceptualization of the manuscript and to the statistical analyses. CT contributed to the conceptualization of the manuscript and wrote the manuscript. All authors read and approved the final manuscript.

#### Funding

This research received no specific grant from any funding agency in the public, commercial, or not-for-profit sectors.

#### Data availability

Data used were obtained from the ADNI database ([adni.loni.usc.edu](http://adni.loni.usc.edu)). ADNI was launched in 2003 as a public-private partnership, led by Principal Investigator Michael W. Weiner, MD. The primary goal was to test whether serial MRI, positron emission tomography, other biological markers, and clinical and neuropsychological assessment can be combined to measure the progression of MCI and early Alzheimer's disease. For more information, see [www.adni-info.org](http://www.adni-info.org). Publicly available datasets were analyzed in this study. This data can be found here: <http://adni.loni.usc.edu/>. Data used in the preparation of this article were obtained from Alzheimer's Disease Neuroimaging Initiative (ADNI) database ([adni.loni.usc.edu](http://adni.loni.usc.edu)). As such, the investigators within the ADNI contributed to the design and implementation of ADNI and/or provided data but did not participate in the analysis or writing of this report. A complete listing of ADNI investigators can be found at: [http://adni.loni.usc.edu/wp-content/uploads/how\\_to\\_apply/ADNI\\_Acknowledgement\\_List.pdf](http://adni.loni.usc.edu/wp-content/uploads/how_to_apply/ADNI_Acknowledgement_List.pdf).

#### Declarations

##### Ethics approval and consent to participate

As per ADNI protocols, all procedures performed in studies involving human participants were in accordance with the ethical standards of the institutional and/or national research committee and with the 1964 Helsinki Declaration

and its later amendments or comparable ethical standards. More details can be found at <http://adni.loni.usc.edu/>. This article does not contain any studies with human participants performed by any of the authors.

#### Consent for publication

The authors received the consent of publication from ADNI.

#### Competing interests

CT is a member of the Scientific Editorial Board of *European Radiology Experimental* (section: neuro and head/neck). As such they did not participate in the selection nor review processes for this article. The remaining authors declare that they have no conflict of interest.

#### Author details

<sup>1</sup>Department of Computer Science, University of Pisa, Largo Bruno Pontecorvo 3, 56127 Pisa, Italy. <sup>2</sup>INFN, Division of Bologna, Bologna, Italy. <sup>3</sup>European Institute of Oncology (IEO), Via Adamello 16, 20139 Milano, Italy. <sup>4</sup>Department of Civil, Chemical, Environmental, and Materials Engineering, University of Bologna, via Umberto Terracini 28, 40131 Bologna, Italy. <sup>5</sup>Department of Management, Economics and Industrial Engineering, Politecnico di Milano, Via Lambruschini 4/b, 20156 Milano, Italy. <sup>6</sup>Department of Informatics, Bioengineering, Robotics and Systems Engineering, Università Degli Studi di Genova, via Dodecaneso 35, 16146 Genova, Italy. <sup>7</sup>Department of Physics and Astronomy, University of Bologna, viale Berti Pichat 6/2, 40126 Bologna, Italy. <sup>8</sup>Department of Physiology, Anatomy and Genetics, University of Oxford, Sherrington Building Parks Road, OX13PT Oxford, England.

Received: 3 September 2024 Accepted: 5 February 2025

Published online: 19 March 2025

#### References

- Bastiani M (2012) Human cortical connectome reconstruction from diffusion weighted MRI: the effect. *Neuroimage* 62:1732–1749. <https://doi.org/10.1016/j.neuroimage.2012.06.002>
- Talozzi L, Testa C, Evangelisti S et al (2018) Along-tract analysis of the arcuate fasciculus using the Laplacian operator to evaluate different tractography methods. *Magn Reson Imaging* 54:183–193. <https://doi.org/10.1016/j.mri.2018.08.013>
- Woolrich MW, Jbabdi S, Patenaude B et al (2009) Bayesian analysis of neuroimaging data in FSL. *Neuroimage* 45:173–186. <https://doi.org/10.1016/j.neuroimage.2008.10.055>
- Sporns O (2013) Structure and function of complex brain networks. *Dialog Clin Neurosci* 15:247–262. <https://doi.org/10.31887/DCNS.2013.15.3/osporns>
- Fiscione C, Sighinolfi G, Manners DN et al (2024) Multiparametric MRI dataset for susceptibility-based radiomic feature extraction and analysis. *Sci Data* 11:575. <https://doi.org/10.1038/s41597-024-03418-6>
- Vogt BA, Deepak NP (1987) Cingulate cortex of the rhesus monkey: II. Cortical afferents. *J Comp Neurol* 262:271–289. <https://doi.org/10.1002/cne.902620208>
- Mufson EJ, Deepak NP (1984) Some observations on the course and composition of the cingulum bundle in the rhesus monkey. *J Comp Neurol* 225:31–43. <https://doi.org/10.1002/cne.902250105>
- Catani M, Howard RJ, Pajevic S, Jones DK (2002) Virtual in vivo interactive dissection of white matter fasciculi in the human brain. *Neuroimage* 17:77–94. <https://doi.org/10.1006/nimg.2002.1136>
- Catani M, Thiebaut de Schotten M (2012) Atlas of human brain connections. Oxford University Press, USA
- Singh M, Wong CW (2010) Independent component analysis-based multifiber streamline tractography of the human brain. *Magn Reson Med* 64:1676–1684. <https://doi.org/10.1002/mrm.22509>
- Beckmann M, Johansen-Berg H, Rushworth MF (2009) Connectivity-based parcellation of human cingulate cortex and its relation to functional specialization. *J Neurosci* 29:1175–1190. <https://doi.org/10.1523/JNEUROSCI.3328-08.2009>
- Rudebeck PH, Buckley MJ, Walton ME, Rushworth MF (2006) A role for the macaque anterior cingulate gyrus in social valuation. *Science* 313:1310–1312. <https://doi.org/10.1126/science.1128197>
- Kennerley SW, Walton ME, Behrens TE, Buckley MJ, Rushworth MF (2006) Optimal decision making and the anterior cingulate cortex. *Nat Neurosci* 9:940–947. <https://doi.org/10.1038/nn1724>
- Bettcher BM, Mungas D, Patel N et al (2016) Neuroanatomical substrates of executive functions: beyond prefrontal structures. *Neuropsychologia* 85:100–109. <https://doi.org/10.1016/j.neuropsychologia.2016.03.001>
- Bubb EJ, Metzler-Baddeley C, Aggleton JP (2018) The cingulum bundle: anatomy, function, and dysfunction. *Neurosci Biobehav Rev* 92:104–127. <https://doi.org/10.1016/j.neubiorev.2018.05.008>
- Jones DK, Christiansen KF, Chapman RJ, Aggleton JP (2013) Distinct subdivisions of the cingulum bundle revealed by diffusion MRI fibre tracking: implications for neuropsychological investigations. *Neuropsychologia* 51:67–78. <https://doi.org/10.1016/j.neuropsychologia.2012.11.018>
- Wu Y, Sun D, Wang Y, Wang Y, Ou S (2016) Segmentation of the cingulum bundle in the human brain: a new perspective based on DSI tractography and fiber dissection study. *Front Neuroanat* 10:84. <https://doi.org/10.3389/fnana.2016.00084>
- Cannistraro PA, Makris N, Howard JD et al (2007) A diffusion tensor imaging study of white matter in obsessive-compulsive disorder. *Depress Anxiety* 24:440–446. <https://doi.org/10.1002/da.20246>
- Wise T, Radua J, Nartje G, Cleare AJ, Young AH, Arnone D (2016) Voxel-based meta-analytical evidence of structural disconnectivity in major depression and bipolar disorder. *Biol Psychiat* 79:293–302. <https://doi.org/10.1016/j.biopsych.2015.03.004>
- Tuch DS, Reese TG, Wiegell MR, Makris N, Belliveau JW, Wedeen VJ (2002) High angular resolution diffusion imaging reveals intravoxel white matter fiber heterogeneity. *Magn Reson Med* 48:577–582. <https://doi.org/10.1002/mrm.10268>
- Tournier JD, Calamante F, Connelly A (2012) MRtrix: diffusion tractography in crossing fiber regions. *Int J Imag Syst Tech* 22:53–66. <https://doi.org/10.1002/ima.22005>
- Jeurissen B, Tournier JD, Dhollander T, Connelly A, Sijbers J (2014) Multi-tissue constrained spherical deconvolution for improved analysis of multi-shell diffusion MRI data. *Neuroimage* 103:411–426. <https://doi.org/10.1016/j.neuroimage.2014.07.061>
- Radwan AM, Sunaert S, Schilling K et al (2022) An atlas of white matter anatomy, its variability, and reproducibility based on constrained spherical deconvolution of diffusion MRI. *Neuroimage* 254:119029. <https://doi.org/10.1016/j.neuroimage.2022.119029>
- Zhang H, Schneider T, Wheeler-Kingshott CA, Alexander DC (2012) NODDI: practical in vivo neurite orientation dispersion and density imaging of the human brain. *Neuroimage* 61:1000–1016. <https://doi.org/10.1016/j.neuroimage.2012.03.072>
- Alves GS, Ferrer Carvalho A, de Amorim de Carvalho L et al (2017) Neuroimaging findings related to behavioral disturbances in Alzheimer's disease: a systematic review. *Curr Alzheimer Res* 14:61–75. <https://doi.org/10.2174/1567205013666160603010203>
- Zhou Y, Wei L, Gao S, Wang J, Hu Z (2023) Characterization of diffusion magnetic resonance imaging revealing relationships between white matter disconnection and behavioral disturbances in mild cognitive impairment: a systematic review. *Front Neurosci* 17:1209378. <https://doi.org/10.3389/fnins.2023.1209378>
- Choo IH, Lee DY, Oh JS et al (2010) Posterior cingulate cortex atrophy and regional cingulum disruption in mild cognitive impairment and Alzheimer's disease. *Neurobiol Aging* 31:772–779. <https://doi.org/10.1016/j.neurobiolaging.2008.06.015>
- Nakata Y, Sato N, Nemoto K et al (2009) Diffusion abnormality in the posterior cingulum and hippocampal volume: correlation with disease progression in Alzheimer's disease. *Magn Reson Imaging* 27:347–354. <https://doi.org/10.1016/j.mri.2008.07.013>
- Kantarci K, Murray EM, Schwarz CG et al (2017) White-matter integrity on DTI and the pathologic staging of Alzheimer's disease. *Neurobiol Aging* 56:172–179. <https://doi.org/10.1016/j.neurobiolaging.2017.04.024>
- Bergamino M, Walsh RR, Stokes AM (2021) Free-water diffusion tensor imaging improves the accuracy and sensitivity of white matter analysis in Alzheimer's disease. *Sci Rep* 11:6990. <https://doi.org/10.1038/s41598-021-86505-7>
- Bergamino M, Schiavi S, Daducci A, Walsh RR, Stokes AM (2022) Analysis of brain structural connectivity networks and white matter integrity in

- patients with mild cognitive impairment. *Front Aging Neurosci* 14:793991. <https://doi.org/10.3389/fnagi.2022.793991>
32. Folstein MF, Folstein SE, McHugh PR (1975) "Mini-mental state". A practical method for grading the cognitive state of patients for the clinician. *J Psychiatr Res* 12:189–198. [https://doi.org/10.1016/0022-3956\(75\)90026-6](https://doi.org/10.1016/0022-3956(75)90026-6)
  33. Nasreddine ZS, Phillips NA, Bédirian V et al (2005) The Montreal cognitive assessment, MoCA: a brief screening tool for mild cognitive impairment. *J Am Geriatr Soc* 53:695–699. <https://doi.org/10.1111/j.1532-5415.2005.53221.x>
  34. FMRIB Software Library, Release 6.0 (2018). The University of Oxford. <https://fsl.fmrib.ox.ac.uk/fsl/docs/#/>. Accessed 9 Sept 2023
  35. MRtrix3 (2023) <https://www.mrtrix.org/>. Accessed 20 Sep 2023
  36. Tournier JD, Smith R, Raffelt D et al (2019) MRtrix3: A fast, flexible and open software framework for medical image processing and visualization. *Neuroimage* 202:116137. <https://doi.org/10.1016/j.neuroimage.2019.116137>
  37. Schilling KG, Blaber J, Huo Y et al (2019) Synthesized b0 for diffusion distortion correction (Synb0-DisCo). *Magn Reson Imaging* 64:62–70
  38. Schilling KG, Blaber J, Hansen C et al (2020) Distortion correction of diffusion weighted MRI without reverse phase-encoding scans or field-maps. *PLoS One* 15:e0236418. <https://doi.org/10.1371/journal.pone.0236418>
  39. Garyfallidis E, Brett M, Amirbekian B et al (2014) Dipy, a library for the analysis of diffusion MRI data. *Front Neuroinform* 8:8. <https://doi.org/10.3389/fninf.2014.00008>
  40. Tournier JD, Calamante F, Connelly A (2010) Improved probabilistic streamlines tractography by 2nd order integration over fibre orientation distributions. In: *Proceedings of the International Society for Magnetic Resonance in Medicine*, 1670. John Wiley & Sons, Inc, New Jersey, NJ
  41. Fiscone C, Rundo L, Lugaresi A (2023) Assessing robustness of quantitative susceptibility-based MRI radiomic features in patients with multiple sclerosis. *Sci Rep*. 13:16239. <https://doi.org/10.1038/s41598-023-42914-4>
  42. Benjamini Y, Hochberg Y (1995) Controlling the false discovery rate: a practical and powerful approach to multiple testing. *J R Stat Soc B* 57:289–300. <https://doi.org/10.1111/j.2517-6161.1995.tb02031.x>
  43. Heilbronner SR, Haber SN (2014) Frontal cortical and subcortical projections provide a basis for segmenting the cingulum bundle: implications for neuroimaging and psychiatric disorders. *J Neurosci* 34:10041–10054. <https://doi.org/10.1523/JNEUROSCI.5459-13.2014>
  44. Testa C, Evangelisti S, Popeo M et al (2017) The effect of diffusion gradient direction number on corticospinal tractography in the human brain: an along-tract analysis. *MAGMA* 30:265–280. <https://doi.org/10.1007/s10334-016-0600-1>
  45. Casey KL, Minoshima S, Berger KL, Koeppe RA, Morrow TJ, Frey KA (1994) Positron emission tomographic analysis of cerebral structures activated specifically by repetitive noxious heat stimuli. *J Neurophysiol* 71:802–807. <https://doi.org/10.1152/jn.1994.71.2.802>
  46. Tuladhar AM, van Norden AGW, de Laat KF et al (2015) White matter integrity in small vessel disease is related to cognition. *Neuroimage Clin* 7:518–524. <https://doi.org/10.1016/j.nicl.2015.02.003>
  47. Skandalakis GP, Komaitis S, Kalyvas A et al (2020) Dissecting the default mode network: direct structural evidence on the morphology and axonal connectivity of the fifth component of the cingulum bundle. *J Neurosurg* 134:1334–1345. <https://doi.org/10.3171/2020.2.JNS193177>
  48. Metzler-Baddeley C, Jones DK, Stevenon J, Westacott L, Aggleton JP, O'Sullivan MJ (2012) Cingulum microstructure predicts cognitive control in older age and mild cognitive impairment. *J Neurosci* 32:17612–17619. <https://doi.org/10.1523/JNEUROSCI.3299-12.2012>
  49. Yamamoto M, Kushima I, Kimura H et al (2015) White matter micro-structure between the pre-SMA and the cingulum bundle is related to response conflict in healthy subjects. *Brain Behav* 5:e00375. <https://doi.org/10.1002/brb3.375>
  50. Fox MD, Snyder AZ, Vincent JL, Corbetta M, Van Essen DC, Raichle ME (2005) The human brain is intrinsically organized into dynamic, anticorrelated functional networks. *Proc Natl Acad Sci USA* 102:9673–9678. <https://doi.org/10.1073/pnas.0504136102>
  51. Chrastil ER, Sherrill KR, Hasselmo ME, Stern CE (2015) There and back again: hippocampus and retrosplenial cortex track homing distance during human path integration. *J Neurosci* 35:15442–15452. <https://doi.org/10.1523/JNEUROSCI.1209-15.2015>
  52. Halliday G (2017) Pathology and hippocampal atrophy in Alzheimer's disease. *Lancet Neurol* 16:862–864. [https://doi.org/10.1016/S1474-4422\(17\)30343-5](https://doi.org/10.1016/S1474-4422(17)30343-5)
  53. Mitolo M, Zoli M, Testa C et al (2022) Neuroplasticity mechanisms in frontal brain gliomas: a preliminary study. *Front Neurol* 13:867048. <https://doi.org/10.3389/fneur.2022.867048>
  54. Zoli M, Talozzi L, Martinoni M et al (2021) From neurosurgical planning to histopathological brain tumor characterization: potentialities of arcuate fasciculus along-tract diffusion tensor imaging tractography measures. *Front Neurol* 12:633209. <https://doi.org/10.3389/fneur.2021.633209>

## Publisher's Note

Springer Nature remains neutral with regard to jurisdictional claims in published maps and institutional affiliations.